

2.3.3 Velocity channel analysis

3.2.2 Second-order Structure Functions

We use the procedure described in Section ?? to calculate velocity centroid maps for the $H\alpha$, $[O\text{ III}]\lambda 5007$, $[N\text{ II}]\lambda 6584$ and also $[S\text{ II}]\lambda 6716$ emission lines and then calculate the corresponding second-order structure functions according to Equation ?. Results for representative evolutionary times are shown in Figures A1 to A3 of Appendix A, where power law fits to the slope (m_{2D}) of the structure function are carried out for the inertial range of scales.

In Figure 6 we show the evolution of m_{2D} with time for the different lines and for the three principal viewing directions of the simulation cube. For the line of sight along the z -axis (first column of Fig. 6), one sees for all lines a consistent steepening of the structure function graph with time (increase in m_{2D}). But for other viewing directions no such trend is apparent: both rising and falling behavior of m_{2D} is seen, with little consistency between different lines.

In order to understand why one particular viewing direction is different, we produced histograms of the emission-line velocity centroid values binned into narrow $< 2 \text{ km s}^{-1}$ bins for the three different lines of sight at the four different times. The histograms are presented in Figure 7, from which we see that for the z -axis line of sight, the values of V_c are not distributed symmetrically about the mean value and, in fact, for the $H\alpha$ and $[O\text{ III}]\lambda 5007$ emission lines, a “wing” develops for negative values of V_c that extends to more negative values as time progresses. This tendency is not seen for the y - and x - axis lines of sight. We attribute this wing to a “champagne” flow towards the observer along the z -axis. This flow would be perpendicular to the line of sight for observations along the other axes.

3.2.3 Velocity Channel Analysis

Figure 8 shows the evolution with time of the VCA slope from thin and thick channels (shown by filled circle and cross symbols, respectively) for different ions and for different viewing directions. The individual VCA power spectra from which these slopes were extracted are presented in Appendix B. It can be seen that both γ_t and γ_T are remarkably stable with time during the latter part of the evolution ($t > 200,000$ years). Although thermal broadening means that there is no clear distinction between γ_t and γ_T for the $H\alpha$ line, the two values are clearly distinguished for the heavier ions, with the thin slices showing a significantly shallower slope, especially for $[O\text{ III}]$. The implications for diagnosing turbulence statistics are discussed in § 4.1.3.

4.1.2 Structure Function

The structure function of the velocity centroids is an observationally attractive diagnostic because it is relatively immune to the effects of thermal broadening and poor spectral resolution, so long as sufficiently high signal-to-noise spectra are used. However, it has the disadvantage that relating the observed slope to the 3-dimensional velocity statistics depends on the geometry of the emitting region, see § ?. For transverse separations larger than the characteristic line-of-

sight depth of the emitting gas, the two-dimensional gradient should be equal to the three-dimensional one:

$$m_{2D} = m_{3D} = -3 - n,$$

whereas at smaller separations than this, projection smoothing, as described above, means that the two-dimensional gradient is steeper:

$$m_{2D} = 1 + m_{3D} = -2 - n.$$

Based on our simulation’s velocity power spectrum index at late times of $n \approx -3.2$ (see Figs. ?? and ??), the structure function slope should be $m_{2D} = 0.2$ in the large-scale limit and $m_{2D} = 1.2$ in the small-scale limit.

In fact, all of the measured slopes lie between these two limits, with a systematically increasing value from low to high-ionization lines: $m_{2D}([S\text{ II}]) = 0.33 \pm 0.02$, $m_{2D}([N\text{ II}]) = 0.49 \pm 0.03$, $m_{2D}(H\alpha) = 0.59 \pm 0.04$, $m_{2D}([O\text{ III}]) = 0.74 \pm 0.04$, where the averages were performed for $t > 200,000$ years. This is qualitatively consistent with expectations because the emission from lower-ionization lines is confined to thin layers near the ionization front, whereas higher ionization emission is more distributed over the volume and therefore subject to greater projection smoothing.

If the line-of-sight depth were constant over the face of the $H\text{ II}$ region, then the structure function would show a break at a scale equal to that depth, but in reality the depth varies from point to point, so there will not be a sharp break. Instead, the structure function is expected to show negative curvature, with the gradient gradually decreasing as one passes from smaller to larger scales. A small such effect is seen in the structure functions derived from our simulations (Fig. A1 to A3): the fit to a power law is generally not so good as in the case of the power spectra, with negative residuals at both ends of the fitted range, indicative of a negative curvature. That the observed effect is so small is probably due to the fact that the distribution of line-of-sight depths strongly overlaps with the limited dynamic range in separations available from our simulations, bounded at small scales by numerical dissipation, and at large scales by the size of the ionized region.

It is disappointing that none of the measured slopes reach either of the limiting cases discussed above. All that can be deduced from the structure function is that $1 + m_{3D} > m_{2D}([O\text{ III}])$ and $m_{3D} < m_{2D}([S\text{ II}])$, which implies $n = -2.74$ to -3.33 . Although this is a rather wide range of allowed velocity power spectrum slopes, it does serve to clearly rule out the Kolmogorov value of $n = -3.667$. Furthermore, the “true” value of $n = -3.12 \pm 0.03$ lies close to the middle of the allowed range.

A further proviso to the use of the structure function is that systematic anisotropic flows can affect the measured slopes when the viewing angle is along the direction of the flow. Such an effect is seen at later times for our simulation when viewed along the z -axis (Fig. A1). In this case, the structure function tends to steepen at the large-scale end of our fitting range, producing a positive curvature, which is opposite to the more typical case of negative curvature discussed above. Such cases may also be identified by the presence of a significant skew in the PDF of the line-of-sight velocity (see Fig. 7).

Figure 9 illustrates these points by graphing the correlation between the structure function slope m_{2D} and the slope

Figure 6. Evolution of second-order structure function power-law index, m_{2D} , as a function of time. From top to bottom: $H\alpha$, $[O III]\lambda 5007$, $[N II]\lambda 6584$, $[S II]\lambda 6716$. From left to right: line of sight along the z , x and y axes, respectively.

Figure 7. Histograms of velocity centroid values for each emission line along different lines of sight. From top to bottom: $H\alpha$, $[O III]\lambda 5007$, $[N II]\lambda 6584$, $[S II]\lambda 6716$. From left to right: line of sight along the z , x and y axes, respectively. The different line types refer to different times: thick, grey line—150,000 yrs, dashed line—200,000 yrs, short-dashed line—250,000 yrs, continuous black line—300,000 yrs.

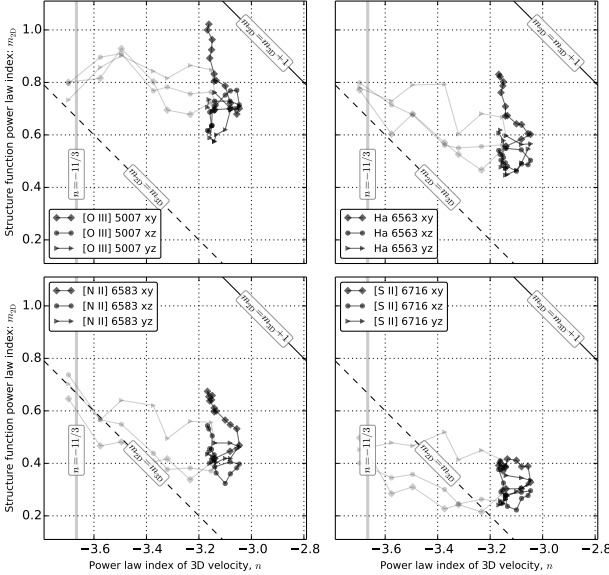


Figure 9. Structure function slope versus velocity power law slope. Each panel shows a different emission line; clockwise from upper left: $[O III]$, $H\alpha$, $[S II]$, $[N II]$. Structure function slopes are shown for the 3 principal viewing directions, distinguished by different symbol types (see key). Dim gray lines and symbols show evolutionary times $< 200,000$ years, while black lines and symbols show times $> 200,000$ years.

n of the underlying 3D velocity fluctuations. The theoretical relation is shown by black diagonal lines, both with (continuous line) and without (dashed line) projection smoothing. It is apparent that a large part of the variation in m_{2D} is not driven by changes in n . Indeed, m_{2D} shows a larger or equal variation in the latter stages of evolution, when n is approximately constant, than it does in the earlier stages, when n is varying.

Note that the additional complication identified by ?, whereby correlations between density and velocity fluctuations affect the translation between m_{2D} and n , is likely of minor importance in our case. ? show that this is most important for high Mach number turbulence, where $\delta\rho/\langle\rho\rangle > 1$, whereas the transonic turbulence inside our simulated H II regions produces more modest density contrasts.

4.1.3 Velocity Channel Analysis

The velocity channel analysis consists of calculating the two-dimensional power spectrum of the brightness distribution in isovelocity channels of varying thickness. We consider two cases: thick slices, which are wide enough ($\sim 100 \text{ km s}^{-1}$) to include all the emission in the line, and thin slices, with width 5 km s^{-1} . Because the velocity spectrum in our sim-

ulations is rather shallow (see above), the line-of-sight turbulent velocity dispersion δv exceeds the width of these thin slices over the full range of length scales that we can usefully study, from 0.1 pc ($\delta v \approx 8 \text{ km s}^{-1}$) to 1 pc ($\delta v \approx 10 \text{ km s}^{-1}$). Figure 10 shows typical examples of the $[O III]$ brightness in thick and thin slices.

To use thinner slices would not be useful for a variety of reasons. First, 5 km s^{-1} corresponds to the highest resolution that can be achieved with optical spectrographs that are optimised for studying extended sources, such as Keck HIRES or VLT UVES. Second, thinner slices are increasingly subject to “shot noise” due to the finite resolution of the numerical simulations, which produces spurious small-scale power, as discussed by ? and ?. Third, thermal broadening would smoothe out any structure on scales $< 5 \text{ km s}^{-1}$ for all but the heaviest ions.

The procedure for deriving the power-law index of the velocity fluctuations from the velocity channels is slightly different, depending on whether the power spectrum of the emissivity fluctuations is “steep” or “shallow” (see above). In the steep case, which applies to $[O III]$ in our simulation, the slope of the average power spectrum of the brightness maps in the thin isovelocity channels is given by $\gamma_{\text{thin}} = -3 + \frac{1}{2}m_{3D}$, where $m_{3D} = -3 - n = 0.2 \pm 0.1$ for our simulation. The derived value from the $[O III]$ thin channel maps is $\gamma_{\text{thin}} = -2.84 \pm 0.11$, which compares very well with the value -2.9 ± 0.05 that is implied by the simulation’s value of n .

In the shallow case, it is the difference in slope between the thin and thick slices that is predicted to depend on the velocity fluctuations: $\gamma_{\text{thin}} - \gamma_{\text{thick}} = \frac{1}{2}m_{3D}$. The derived values are $\gamma_{\text{thin}} - \gamma_{\text{thick}} = 0.08 \pm 0.04$, 0.18 ± 0.04 , and 0.18 ± 0.04 for $H\alpha$, $[N II]$, and $[S II]$, respectively. These also compare well with the value of 0.1 ± 0.05 that is implied by the simulation’s value of n .

The slopes of the power spectra of the thick slices themselves, which are simply the velocity-integrated surface brightness images* are predicted (?) to be equal to the slopes of the 3D power spectra of their respective emissivities. However, only in the case of $[O III]$ do we find this to be the case. In the case of the other lines, γ_{vthick} is shallower than the emissivity’s spectral index n by 0.36 , 0.19 , 0.61 for $H\alpha$, $[N II]$, and $[S II]$, respectively. The reason for this discrepancy may be the increasingly “sheet-like” morphology of the emission in the lower ionization lines. As shown in § 4.1 of ?, one should see a transition from $\gamma_{\text{vthick}} = n$ to the shallower slope $\gamma_{\text{vthick}} = n + 1$ at transverse scales larger than the line-of-sight depth of the emitting region.

* Although for simplicity, extinction is not included.

Figure 8. Evolution of velocity channel power-law index as a function of time for thick channels (γ_T ; crosses) and thin channels (γ_t ; filled circles). From top to bottom: $H\alpha$, $[O III] \lambda 5007$, $[N II] \lambda 6584$, $[S II] \lambda 6716$. From left to right: line of sight along the z , x and y axes, respectively. Thermal broadening was included in all cases.

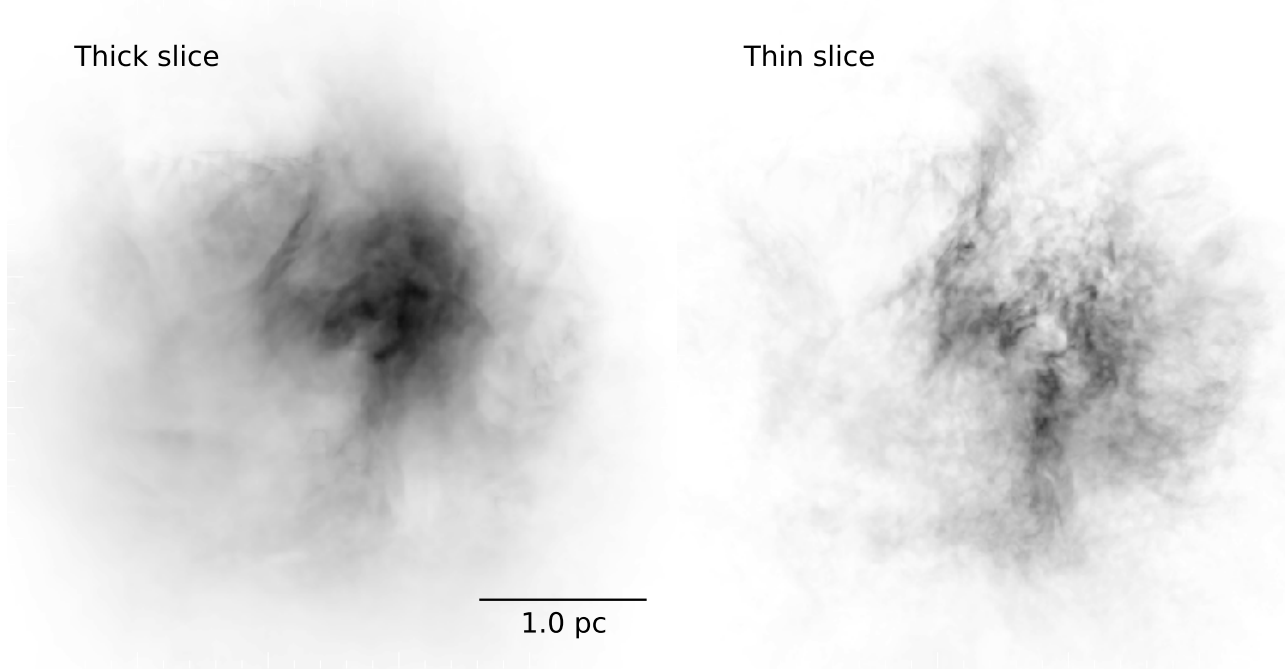


Figure 10. Surface brightness maps in thick (left) versus thin (right) velocity slices for the $[O III]$ line from our simulation at an age of 300,000 years. The thick slice covers the full velocity range of the emission line, while the thin slice has a width of 5 km s^{-1} , which is smaller than the turbulent velocity fluctuations, but slightly larger than the thermal broadening for this line. It is apparent that the thin slice shows considerably greater small-scale structure than the thick slice, which is reflected in its shallower power spectrum. The brightness structure in the thick slice is due entirely to the emissivity fluctuations within the $H II$ region, whereas the additional structure in the thin slice is caused by velocity fluctuations.

APPENDIX A: EXAMPLE SECOND-ORDER STRUCTURE FUNCTIONS OF THE LINE-OF-SIGHT VELOCITY CENTROIDS

Figures A1 to A3 show the second-order structure functions of the line-of-sight velocity centroid maps (see §§ 4.1.2 and ??) for the four emission lines at the four evolutionary times depicted in Figure ?. If turbulence is present, the second-order structure function should exhibit an inertial range over which it is a power law with length scale. Accordingly, we perform a least-squares fit to the data points. However, it is not immediately clear what the limits for the fit should be. At small scales, the lower limit for the inertial range should be defined by the scale at which numerical dissipation effects cease to be important (?). For the present simulations, we tested several values and the size scale equivalent to 8 computational cells proved to be adequate for all emission lines and evolution times studied. For the upper limit, we examined the projected emission maps and calculated the area occupied by the pixels having greater than 6.6% of the peak intensity. We then took the radius of the circle having the same area to be the upper limit for the least-squares fit. This procedure appears to work very well, as can be seen in Figures A1 and A3. If a different line of sight is chosen, the radius of this circle will be different and needs to be calculated self-consistently for every projection. Note that the

inertial range for each combination of line and view tends to become broader with time due to the expansion of the $H II$ region. At the latest time, 300,000 yrs, both the $H\alpha$ and $[O III] \lambda 5007$ structure functions appear to develop a break, which would be better fit by two power laws, one below a scale of about 0.3 pc and a steeper one for larger scales. However, we have fit just a single power law to both of these cases.

An alternative criterion for the upper limit was used by ? who used the theoretical result for homogeneous turbulence that decorrelation of the second-order structure function occurs when the auto-correlation function changes sign from positive to negative. This corresponds approximately to the scale for which the second-order structure function is equal to 2. However, as can be seen from Figures A1 and A3, for many of our emission lines this criterion cannot be used, since the structure function nowhere rises above 2.

APPENDIX B: EXAMPLE POWER SPECTRA FROM VELOCITY CHANNEL ANALYSIS

Figures ?? to ?? show the power spectra resulting from the velocity channel analysis (see § 2.3.3). Each of the three figures is for a different viewing direction and shows the four emission lines at four different times. For each com-

Figure A1. Second-order structure functions against length scale for projection onto the xy -plane. From top to bottom: $H\alpha$, $[O\text{ III}]\lambda 5007$, $[N\text{ II}]\lambda 6584$, $[S\text{ II}]\lambda 6716$. From left to right: 150,000, 200,000, 250,000 and 300,000 years. The points represent the calculated structure function for the numerical simulation. The solid line is the least-squares fit to the data points between limits described in the text, represented by the grey rectangle. The horizontal dotted line at $\log 2$ is included as a reference value.

Figure A2. Same as Fig. A1 but for a projection onto the xz plane.

bination of line and time, there are two panels: an upper panel without including thermal Doppler broadening and a lower panel with the broadening effects included. In each graph, two power spectra are plotted: one representing a very thick velocity slice (i.e., encompassing all the emission) and the other averaged over thin velocity slices of width $\delta v \sim 5 \text{ km s}^{-1}$. Also shown are the least-squares power-law fits to the thin and very thick slice spectra and the range in wavenumber over which the fit is calculated. This wavenumber range corresponds to the length-scale range used for the structure function fits (see § 3.2.2). The very thick velocity slice is equivalent to the total intensity along the line of sight and its power spectrum does not vary with the addition of thermal broadening.

It is clear that the thermal broadening has a large effect on the VCA of the $H\alpha$ line, effectively erasing the difference in slope between the thin and thick slices. For photoionized gas at $T_e = 10^4 \text{ K}$, the FWHM of the $H\alpha$ line is $\sim 22 \text{ km s}^{-1}$, while that of an oxygen line is a quarter of this, $\sim 5.5 \text{ km s}^{-1}$. Indeed, the heavier ions are less affected by thermal broadening, but a slight steepening of the thin-slice power spectra can still be seen, amounting to a reduction in γ_t of ~ 0.1 .

For the thermally broadened case, the variation with time of the slopes of these fits, γ_T for the thick slices and γ_t for the thin slices, is shown in Fig 8 and discussed in § 3.2.3.

Figure A3. Same as Fig. A1 but for a projection onto the yz -plane.